ACS APPLIED MATERIALS & INTERFACES

www.acsami.org

Research Article

Self-Assembled Monolayers for Improved Charge Injection of Silver Back Electrodes in Inverted Organic Electronic Devices

Sneha Sreekumar, Marzieh Heidari, Zhongkai Cheng, Hemanth Maddali, Krystal House, Heinz Frei, Elena Galoppini,* and Deirdre M. O'Carroll*

Cite This: *ACS Appl. Mater. Interfaces* 2022, 14, 38270–38280

Read Online

ACCESS | Metrics & More | Article Recommendations | Supporting Information

ABSTRACT: Self-assembled monolayers (SAMs) formed from thiol compounds bound to Ag and Au electrodes have been used as an important strategy in improving the stability and efficiency of optoelectronic devices. Thiol compounds provide only one binding site with the metal electrode which limits their influence. Dithiolane/dithiol compounds can provide multiple binding sites and could be useful in enhancing the performance of the device. In this study, inverted organic semiconducting hole-only devices were fabricated by using Ag back electrodes in conjunction with SAMs formed from disulfide lipoic acid-based compounds and were compared to a long aliphatic chain thiol. The binding and the electronic properties as well as electrical characteristics of the SAMs on silver were studied to look at the influence of their structure on charge injection in the organic semiconductor devices. It was found that the SAMs formed with (±)-α-lipoic acid, isolipoic acid, and (±)-4-phenylbutyl 5-(1,2-dithiolan-3-yl) pentanoate significantly improved the charge injection by either changing the work function of the Ag or altering the physical interaction between the polymer and the metal surface. This study may lead to an understanding of how the nature of the functional groups of the SAM and the number of bonds formed between each SAM molecule and the metal electrode influence the contact resistance and the performance of organic semiconductor devices.

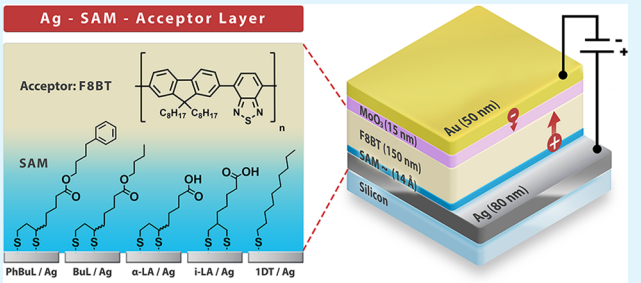

KEYWORDS: *self-assembled monolayers, organic semiconductors, lipoic acid, silver electrodes, inverted devices, thiols, dithiolanes*

1. INTRODUCTION

Organic semiconductors are of considerable interest for a wide range of electronic and optoelectronic devices including organic field-effect transistors (OFETs), sensors, light-emitting diodes (LEDs) and photovoltaics (PVs).[1−7] In the field of organic optoelectronics, device efficiency and device stability are the most important and critical issues. In the past decades, many strategies have been developed to enhance the efficiencies of organic optoelectronic devices, including incorporation of additives in the active layer;[8−10] addition of specific interfacial layers between the semiconductor and the electrodes,[10] and development of new device architectures.[11−14] Additionally, organic optoelectronic devices have shown increased stability when moisture-sensitive interfacial materials, such as PEDOT:PSS, are replaced with more stable metal oxide interfacial layers.[11,12,14,15]

There are two general methods for the fabrication of organic semiconductor optoelectronic devices: the first fabrication method involves ITO/glass electrodes with metal electrode deposition as the last step (conventional fabrication); the second method involves building the device on top of the metal electrode (inverted fabrication).[16,17] The conventional fabrication method is ubiquitous for organic optoelectronic devices because ITO/glass has high transparency, high work function, and good conductivity. Disadvantages of the conventional fabrication method include the rigidity, high cost, and high embodied energy of ITO as well as the difficulty in controlling the morphology of the surface of the metal electrode that is deposited on top of the semiconductor/interfacial layers.

Furthermore, it is advantageous to be able to control the surface morphology of metal electrodes in contact with the semiconductor layer, because, metals are playing an increasingly important role in promoting optimal light management in thin-film optoelectronic devices. For example, gratings are often imprinted into the organic layer prior to depositing the metal layer in OLED devices to outcouple surface plasmon polaritons that would otherwise significantly reduce light extraction efficiency.[18] Therefore, the morphology of the metal electrode is highly dependent on the surface morphology of the organic semiconductor layer, which is known to vary

Received: May 2, 2022
Accepted: July 1, 2022
Published: July 19, 2022

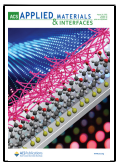

https://doi.org/10.1021/acsami.2c07610
ACS Appl. Mater. Interfaces 2022, 14, 38270−38280

substantially depending on processing conditions. As a result, control of the metal electrode morphology is not possible with the conventional fabrication method for organic optoelectronic devices.

The inverted fabrication method allows control of the structure and morphology of the metal surface to achieve a variety of photonic and plasmonic behavior in devices.[19−22] Different metals, including Au, Al, Ag, and Cu, can play significant roles in light management because they can support surface plasmons at different wavelengths in the visible and near-infrared ranges. In particular, Ag serves as an excellent electrode for optoelectronic devices because of its low optical loss (absence of interband electronic absorption in the visible spectral range), high reflectivity, and high conductivity.[16−20] However, the work function of Ag (∼4.4 eV) often does not match well with either of the frontier orbital energies of the organic semiconductor.[23,28] Therefore, Ag electrodes must be used in combination with a suitable interfacial layer to minimize barriers to electron or hole collection and to improve adhesion and interaction with the organic semiconductor. Finally, it is difficult to maintain a pristine Ag surface during fabrication and operation because of surface oxidation or adsorption of impurities. Therefore, it is essential to find interfacial layers that can passivate Ag while enabling charge transport to/from the organic semiconductor.

Self-assembled monolayers (SAMs) have been investigated as interfacial layers between metal electrodes and organic semiconductors for reducing contact resistance in OFET devices.[24,25] For example, Cheng et al. used thiol-based SAMs to investigate the electron and hole injection in poly(9,9-dioctylfluorene-*alt*-benzothiadiazole) (F8BT) OFETs.[27] They showed simultaneous improvement of both electron and hole injection, which was attributed to interface tunneling, modifications of interfacial morphology, interface electronic structure, and changes in the F8BT layer thickness. Kim et al. employed pentafluorobenzenethiol (PFBT) on Au, Ag, and Cu metal electrodes in small-molecule bottom-contact OFETs, and the decoupled contributions from morphological and energetic effects of the SAM on device performance were studied.[29] In these examples, and most other cases that have used SAM-modified metal electrodes in OFET devices, almost all SAMs used have been prepared from thiols (R−SH) that bind via a single sulfur−metal bond.[29] Multiple sulfur−metal binding sites could provide additional stability and influence the SAM structure, for instance, binding angle and therefore chain packing. Additionally, synthetic modifications of the molecules composing the SAM have not been widely investigated. Moreover, while the introduction of a SAM is a relatively straightforward step in the fabrication of an organic (opto)electronic device, it is not obvious whether the thermal and operational stability of the device with a SAM can be comparable to that of interfacial layers made from metal oxides or 2D-materials (e.g., MoO_3, ZnO, graphene, etc.).

In the present work, we have systematically compared the role of five different SAMs on the charge injection and stability of silver electrodes used in inverted organic electronic devices. The SAMs are composed of (±)-α-lipoic acid (α-LA), isolipoic acid (i-LA), (±)-butyl 5-(1,2-dithiolan-3-yl)pentanoate (BuL), (±)-4-phenylbutyl 5-(1,2-dithiolan-3-yl) pentanoate (PhBuL), and 1-decanethiol (1DT) (Figure 1). They differ in the number of binding sites (thiol vs 1,2-dithiolane), the capping groups on the chain (alkyl chain, carboxylic acid, alkyl ester, or ester with an aromatic group), and the chain orientation (α-LA vs i-LA),[30] providing a first probe of the role of an organic monolayer interfacing silver and a conjugated polymer semiconductor, F8BT. The i-LA was synthesized as shown in Scheme S1 and as described in the Experimental Section.[30] PhBuL and BuL were prepared by esterification of the commercially available racemic α-LA.[31] Our hypothesis is that when LA-based SAMs with double attachments are used on Ag back electrodes, the functional group of the SAM and its interaction with the F8BT polymer influence the electrical performance of F8BT diodes (Figure 2a−d).

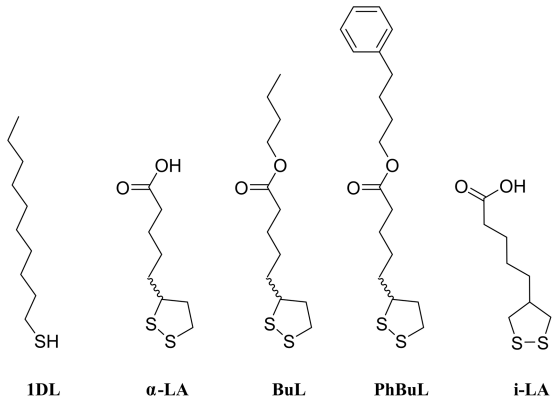

Figure 1. Compounds used to form SAMs on silver electrodes.

2. EXPERIMENTAL SECTION

2.1. Materials and Characterization. Poly(9,9-dioctylfluorene-*alt*-benzothiadiazole) (F8BT; weight-average molecular weight of 104 kg mol^{-1}), 1-decanethiol, (±)-α-lipoic acid, and other reagents and solvents were purchased from Sigma-Aldrich and used without further purification. All air- and moisture-sensitive reactions were performed under a nitrogen atmosphere and in oven-dried glassware. Column chromatography was performed on silica gel (particle size 40−63 μm, pore size ∼60 Å). Thin layer chromatography was performed on silica gel w/UV254 aluminum-backed sheets (200 μm thick) and monitored by UV light (254 nm) or potassium permanganate solution. Fourier-transform infrared (FT-IR) spectra were collected by a Nicolet iS5 FT-IR spectrometer from the neat compounds. NMR spectra were recorded with a Bruker Avance III HD 500 MHz NMR spectrometer. Chemical shifts (δ) are reported relative to TMS (δ 0.00 ppm), and spin−spin coupling constants (*J*) are reported in hertz. Mass spectroscopy was performed by using a Hewlett-Packard GC/MS (GC HP 6870, MS HP 5873) instrument.

Current density−voltage (*J*−*V*) measurements were conducted by using a Keithley 4200A-SCS parameter analyzer. Average values for the current density at 2 V, the turn-on voltage, and the barrier height were obtained from the *J*−*V* measurements of 10 devices for each SAM/Ag and bare Ag electrode type. The standard deviations of the values were also calculated and reported as the error. X-ray photoelectron spectroscopy (XPS) was carried out using a Thermo Scientific K-Alpha X-ray photoelectron spectrometer with a monochromatic Al Kα source (1486.6 eV), hemispherical analyzer, and multichannel detector. The spectra were accumulated at a takeoff angle of 90° with a 0.79 mm^2 spot size at a pressure of $<10^{-8}$ mbar. Ultraviolet photoelectron spectroscopy (UPS) measurements were performed with a Thermo Scientific ESCALAB250 Xi using a He I source (21.2 eV) with a pass energy of 2 eV. The UPS samples were prepared by spin-coating 40 μL of F8BT solution at 4000 rpm for 40 s to obtain 10−20 nm of F8BT on the SAM/Ag surface. The AFM measurements were conducted by using an Asylum Research Cypher ES atomic force microscope operating in amplitude modulation mode or "tapping mode" to obtain both phase and height images. Silicon cantilevers with a spring constant of 9 N/m were used for all the measurements with a tip radius of 7 nm. A scan size of 1 μm^2 with a

https://doi.org/10.1021/acsami.2c07610
ACS Appl. Mater. Interfaces 2022, 14, 38270−38280

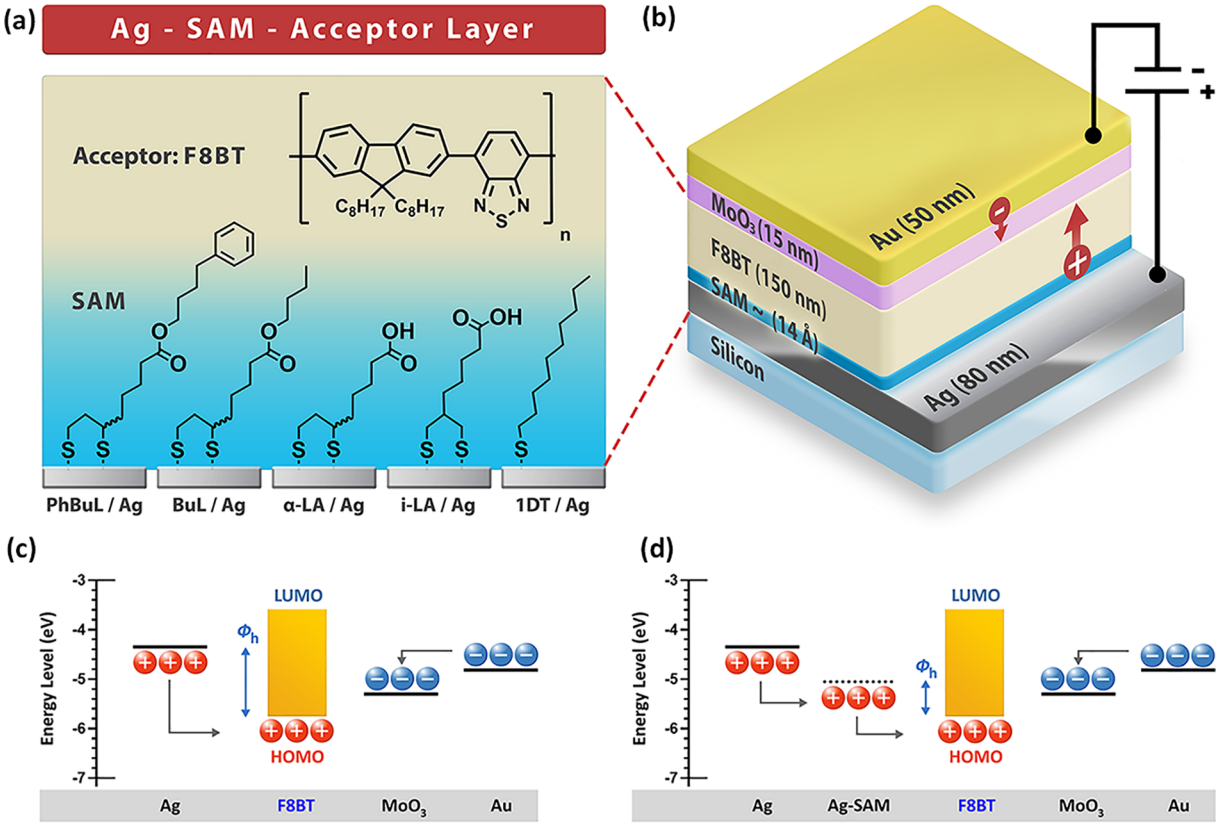

Figure 2. (a, b) Schematics of inverted F8BT hole-only diode with a SAM on the Ag back electrode. (c, d) Energy level diagrams of the diode without and with SAM, respectively. Φ_h is the barrier for hole injection between the Ag or SAM/Ag layer and the HOMO of F8BT. The negative terminal of the external applied voltage source is connected to the Au top electrode, and the positive terminal is connected to the Ag bottom electrode. The holes are injected from the Ag side while the electrons are blocked from flowing into the F8BT layer from the MoO_3 side (i.e., hole-only device operation).

digital resolution of 256 lines × 256 points and a scan rate of 2.44 Hz were used. All Raman spectra were acquired on a Renishaw InVia dispersive Raman spectrometer equipped with a Leica DM microscope and a Renishaw HeNe 633 nm laser (8.5 mW). The samples were viewed by using a 100× objective; for spectral acquisition the exposure time was 10 s, and the number of accumulations was five for a total acquisition time of 50 s. Contact angle measurements were taken by using a Rame-Hart 100-00 goniometer. Fourier-transform infrared reflection-absorption spectroscopy (FT-IRRAS) was carried out with a Bruker FT-IR spectrometer (model Vertex 80) equipped with a computer-controlled reflection accessory Bruker model A513/QA and a wire-grid polarizer model F350. The mirror angle was fixed at 80°, the grid polarizer was switched between p and s polarization, and an aperture of 2.5 mm was used. For each spectral trace, 20 spectra of 200 scans each at 2 cm^{-1} resolution were recorded and averaged.

2.2. Synthesis of BuL and PhBuL.[31] Butanol (for the preparation of BuL) or 4-phenyl-1-butanol (for the preparation of PhBuL) (12.0 mmol) was added in one portion to a stirred solution of (±)-α-lipoic acid (12.0 mmol) in dichloromethane (60 mL) under a nitrogen atmosphere at room temperature. The resulting yellow solution was stirred for 15 min at 0 °C (ice/water bath) under N_2. 1-Ethyl-3-(3-(dimethylamino)propyl)carbodiimide (EDC, 24.0 mmol) and 4-(*N*,*N*-dimethylamino)pyridine (DMAP, 3.6 mmol) in dichloromethane (60 mL) were added, and the solution was stirred for additional 15 min at 0 °C. The cooling bath was removed, and the yellow solution was stirred for 60 h at room temperature. Water (100 mL) was added to the solution, the organic layer was separated, dried over $MgSO_4$, filtered, and the solvent was removed *in vacuo*. The crude product was purified by silica gel column chromatography (ethyl acetate/hexane; 1/5) to yield BuL (80%) or PhBuL (85%) as a yellow oil. BuL: ν_{max} 2954, 2932, 2866, 1732, 1456, 1240, 1168, 1058, 731, 446 cm^{-1}. ^{1}H NMR ($CDCl_3$): δ 4.07 (2H, t, J = 6.7, OCH_2), 3.62−3.52 (1H, m, CH_2), 3.23−3.07 (2H, m, CH_2), 2.51−2.42 (1H, m, CH), 2.31 (2H, t, J = 7.4, CH_2CO), 1.96−1.85 (1H, m, CH_2), 1.77−1.57 (6H, m, CH_2), 1.55−1.33 (4H, m, CH_2), 0.94 (3H, t, J = 7.4, CH_3). ^{13}C NMR ($CDCl_3$): δ 173.6 (C═O), 64.2 (CH_2), 56.3 (CH), 40.2 (CH_2), 38.4 (CH_2), 34.6 (CH_2), 34.1 (CH_2), 30.6 (CH_2), 28.7 (CH_2), 24.7 (CH_2), 19.1 (CH_2), 13.7 (CH_3). *m*/*z*: 262.1 (100.0%), 263.1 (13.0%), 264.1 (9.0%), 265.1 (1.6%). PhBuL: ν_{max} 3023, 2929, 2852, 1726, 1602, 1495, 1453, 1238, 1169, 1064, 747, 695, 571, 474 cm 1. ^{1}H NMR ($CDCl_3$): δ 7.31−7.24 (2H, m, Ph), 7.21−7.15 (3H, m, Ph), 4.09 (2H, t, J = 6.0, OCH_2), 3.59−3.51 (1H, m, CH_2), 3.21−3.04 (2H, m, CH_2), 2.67−2.59 (2H, m, CH_2), 2.49−2.39 (1H, m, CH), 2.31 (2H, t, J = 7.4, CH_2CO), 1.95−1.83 (1H, m, CH_2), 1.76−1.60 (8H, m, CH_2), 1.53−1.39 (2H, m, CH_2). ^{13}C NMR ($CDCl_3$): 173.5 (C), 142.0 (Ph), 128.4 (Ph), 128.3 (Ph), 125.8 (Ph), 64.2 (CH_2), 56.3 (CH), 40.2 (CH_2), 38.5 (CH_2), 35.5 (CH_2), 34.6 (CH_2), 34.1 (CH_2), 28.8 (CH_2), 28.2 (CH_2), 27.8 (CH_2), 24.7 (CH_2). *m*/*z*: 338.1 (100.0%), 339.1 (21.1%), 340.1 (10.8%), 341.1 (1.8%).

2.3. Synthesis of Isolipoic Acid (i-LA).[30] *Diethyl 2-(Hex-5-en-1-yl)malonate (1).* Diethyl malonate (35.0 mmol) was added dropwise over 40 min to a stirred gray suspension of sodium hydride (35.0 mmol of a 60% w/w mixture in mineral oil) in THF (85 mL) at 0 °C (ice/water bath). The resulting pale-yellow solution was stirred for 15 min at 0 °C and then at room temperature for 30 min. A solution of 6-bromo-1-hexene (31.8 mmol) in THF (40 mL) was added, and the gray mixture was stirred at reflux for 18 h. Afterward, the resulting white mixture was cooled to room temperature, and water (15 mL) was added to quench the reaction. Water (100 mL) and ethyl acetate (50 mL) were added, and the organic layer was separated. The organic layer was washed with brine (100 mL), dried over $MgSO_4$, and then filtered. The filtrate was evaporated *in vacuo*.

https://doi.org/10.1021/acsami.2c07610
ACS Appl. Mater. Interfaces 2022, 14, 38270−38280

Silica gel column chromatography (ethyl acetate/hexane; 4/100) (tracked with TLC with potassium permanganate solution; R_f = 0.50) afforded the compound **1** as a colorless oil (79%). ν_{max}: 3020, 2925, 2850, 1725, 1600, 1494, 1451, 1237, 1165, 1060, 748, 697, 578 cm^{-1}. ^1H NMR ($CDCl_3$): δ 5.85−5.72 (1H, m, C<u>H</u>=CH_2), 5.04−4.91 (2H, m, CH=C<u>H</u>$_2$), 4.19 (4H, q, J = 7.3, OC<u>H</u>$_2$$CH_3$), 3.31 (1H, t, J = 7.6, CH), 2.11−1.84 (4H, m, CH_2), 1.48−1.30 (4H, m, CH_2), 1.27 (6H, t, J = 7.3, OCH_2C<u>H</u>$_3$). ^{13}C NMR ($CDCl_3$): 169.55 (C), 138.57 (CH), 114.59 (CH_2), 61.27 (CH_2), 52.05 (CH), 33.41 (CH_2), 28.60 (CH_2), 28.48 (CH_2), 26.78 (CH_2), 14.10 (CH_3).

*2-(Hex-5-en-1-yl)propane-1,3-diol (**2**).* A solution of **1** (25.3 mmol) in anhydrous THF (40 mL) was added in one portion to a stirred gray suspension of lithium aluminum hydride (50.5 mmol) in anhydrous THF (110 mL) at 0 °C (ice/water bath). The resulting mixture was stirred for 30 min at 0 °C and then at rt for 3.5 h. Then anhydrous THF (75 mL) was added to the mixture, and the reaction mixture was cooled to 0 °C. Aqueous NaOH solution (1 M, 3 mL) and water (4 mL) were added. The reaction mixture was stirred vigorously at rt for 16 h. The resulted white mixture was vacuum filtered through Celite and washed with ethyl acetate. The solvents were removed *in vacuo*, and the resulting colorless oil was purified by silica gel column chromatography (ethyl acetate/hexane/methanol; 10/10/2) to give the compound **2** as a colorless oil (75%). ν_{max}: 3332, 2924, 2853, 1640, 1462, 1366, 1243, 1031, 907 cm^{-1}. ^1H NMR ($CDCl_3$): δ 5.86−5.74 (1H, m, C<u>H</u>=CH_2), 5.05−4.90 (2H, m, CH=C<u>H</u>$_2$), 3.86−3.54 (4H, m, C<u>H</u>$_2$OH), 3.11 (2H, s, OH), 2.10−2.01 (2H, m, CH_2), 1.80−1.69 (1H, m, CH), 1.44−1.29 (4H, m, CH_2), 1.27−1.19 (m, 2H, CH_2). ^{13}C NMR ($CDCl_3$): 138.85 (CH), 114.44 (CH_2), 66.19 (CH_2), 41.92 (CH), 33.62 (CH_2), 29.09 (CH_2), 27.57 (CH_2), 26.65 (CH_2).

*2-(Hex-5-en-1-yl)propane-1,3-diyl Dimethanesulfonate (**3**).* To a stirred solution of **2** (20.1 mmol) in CH_2Cl_2 (175 mL), methanesulfonyl chloride (80.5 mmol) was added dropwise over 15 min at 0 °C (ice/water bath), followed by addition of triethylamine (100 mmol). The resulting white mixture was stirred for a further 30 min at 0 °C and, then, for 3 h at room temperature. Then, water (150 mL) was added to the yellow mixture, and the organic layer was separated and washed with brine (150 mL), dried over $MgSO_4$, and then filtered. The filtrate was evaporated under reduced pressure. Silica gel column chromatography (ethyl acetate/hexane; 1/1; R_f = 0.62) afforded compound **3** (94%) as a pale-yellow oil. ν_{max}: 2934, 2864, 1469, 1347, 1331, 1167, 939, 822, 749, 525 cm^{-1}. ^1H NMR ($CDCl_3$): δ 5.85−5.72 (1H, m, C<u>H</u>=CH_2), 5.05−4.91 (2H, m, CH=C<u>H</u>$_2$), 4.24−4.14 (4H, m, CHC<u>H</u>$_2$O), 3.05 (6H, s, SO_2C<u>H</u>$_3$), 2.20−2.12 (1H, m, CH), 2.11−2.01 (2H, m, CH_2), 1.48−1.33 (6H, m, CH_2). ^{13}C NMR ($CDCl_3$): 138.38 (CH), 114.82 (CH_2), 68.26 (CH_2), 38.16 (CH), 37.29 (CH_3), 33.38 (CH_2), 28.65 (CH_2), 26.84 (CH_2), 25.93 (CH_2).

*7-((Methylsulfonyl)oxy)-6-(((methylsulfonyl)oxy)methyl)-heptanoic Acid (**4**).* A solution of **3** (4.9 mmol) in DMF (35 mL) was prepared, and osmium tetroxide (0.05 mmol, 2.5% w/w solution in *t*BuOH) was added. The resulting black mixture was stirred for 5 min at room temperature. Afterward, oxone (12.1 mmol) was added in three portions over 20 min. The resulting brown mixture was stirred vigorously at room temperature for a further 3.5 h. Sodium sulfite (9.3 g) was added, and the resulting mixture was stirred for a further 2 h. Water (100 mL) and aqueous HCl solution (2 M; 25 mL) followed by ethyl acetate:ether (1:1, 100 mL) were added. The organic layer was separated and washed with brine (100 mL), dried over $MgSO_4$, and then filtered. The solvents were evaporated under high vacuum to give compound **4** as a white solid (86%). ν_{max}: 2938, 2867, 1709, 1341, 1330, 1166, 934, 828, 748, 525 cm^{-1}. ^1H NMR ($CDCl_3$): δ 4.32−4.17 (4H, m, CHC<u>H</u>$_2$O), 3.05 (6H, s, SO_2C<u>H</u>$_3$), 2.39 (2H, t, J = 7.2), 2.23−2.14 (1H, m, CH), 1.71−1.62 (2H, m, CH_2), 1.50−1.40 (4H, m, CH_2). ^{13}C NMR ($CDCl_3$): 178.55 (C), 68.07 (CH), 38.02 (CH_2), 37.35 (CH_3), 33.44 (CH_2), 26.68 (CH_2), 25.87 (CH_2), 24.37 (CH_2).

*Isolipoic Acid (**i-LA**).* A stirred solution of **4** (4.2 mmol) in DMF (40 mL) was prepared. Next, sulfur (4.2 mmol) and sodium sulfide hydrate (4.2 mmol) were added. Then the reaction mixture was stirred for 5 h at 85 °C. The mixture was cooled to room temperature. Water (100 mL) was added, and extraction was performed by using ether, followed by washing the organic layer with brine. Then, the organic extract was dried over $MgSO_4$ and filtered. The filtrate was evaporated under high vacuum. Hexane was added, and the yellow precipitate was filtered to afford the isolipoic acid as a yellow solid (76%). ν_{max}: 2924, 2856, 1692, 1463, 1406, 1301, 1257, 1203, 935, 735, 675 cm^{-1}. ^1H NMR ($CDCl_3$): δ 3.25 (2H, dd, J = 11.0, 6.6, CH_2), 2.80 (2H, dd, J = 11.1, 6.7, CH_2), 2.61−2.50 (1H, m, CH), 2.38 (2H, t, J = 7.4, CH_2), 1.72−1.62 (2H, m, CH_2), 1.56−1.50 (2H, m, CH_2), 1.50−1.38 (2H, m, CH_2). ^{13}C NMR ($CDCl_3$): 179.08 (C), 47.59 (CH), 43.95 (CH_2), 33.67 (CH_2), 33.46 (CH_2), 27.97 (CH_2), 24.59 (CH_2). m/z: 206.0 (100.0%), 207.0 (18.6%), 208.0 (14.1%), 209.1 (3.1%).

2.4. Device Fabrication. Silicon substrates were sequentially cleaned with soap water and deionized water in an ultrasonicator for 15 min. The substrates were immersed in a 1:1:5 solution of NH_3, H_2O_2, and deionized water for 20 min at 80 °C and subsequently cleaned with deionized water three times under ultrasonication. The substrates were dried with an air gun and kept under vacuum for an hour. For the bottom electrode, 80 nm of Ag was deposited onto the clean silicon substrates by using a thermal evaporator at a deposition rate of 0.1 nm/s. The Ag-coated substrates were immersed in a 10 mM solution of the compound in isopropanol in the case of α-LA, 1DT, and i-LA or chloroform in the case of BuL and PhBuL. After 1 h, the samples were rinsed with chloroform and dried with an air gun before immediately spin-coating with F8BT solution. A chloroform solution of F8BT (40 μL, 20 mg/mL) was coated on each sample (4000 rpm for 1 min). After spin-coating with F8BT, 15 nm of MoO_3 and 50 nm of Au were thermally evaporated on the F8BT to create the top electrode.

3. RESULTS AND DISCUSSION

The structure of the inverted hole-only devices incorporating the SAMs is depicted in Figure 2a,b. The SAMs are formed on Ag back electrode, and the rest of the device is constructed on top of the SAM/Ag. Energy-level diagrams of devices with and without the SAM layer, showing how the various device layers are expected to influence charge transport, are shown in Figure 2c,d. The positive electrode (anode) is Ag, by which holes are injected and tunnel through the SAM to the HOMO of the F8BT polymer. Au and MoO_3 serve as the negative electrode (cathode) that blocks electrons from being injected into the F8BT (i.e., a hole-only device). The barrier to hole injection (Φ_h) from Ag to F8BT is expected to be altered by the SAM.

3.1. X-ray Photoelectron Spectroscopy (XPS). To further investigate the binding, XPS spectra of the SAMs on Ag were collected (Figure 3). The S2p peaks of the RS−SR bond showed a doublet ($S2p_{3/2}$ and $S2p_{1/2}$) centered at 164 and 165 eV, which shifted to lower binding energies, ∼162 and ∼163 eV in the case of α-LA, upon binding to Ag.[32−34] This spectral change was observed in all XPS spectra of the SAMs on Ag except i-LA/Ag, which showed the S2p peaks associated with binding to Ag at ∼162 and ∼163 eV, in addition to the unbound S−S peaks at 164 and 165 eV. This indicated that i-LA molecules were partially bound to the metal. There were no peaks present for oxidized sulfur, which would have appeared at 167−169 eV.[32] C1s spectra showed that the characteristic peak of the α-LA sp^3 carbon at 285 eV has shifted slightly to 284 eV for α-LA/Ag, i-LA/Ag, and BuL/Ag, which also indicated the binding of α-LA, i-LA, and BuL to the electropositive Ag (Figure S9d). It appeared at 285 eV for PhBuL/Ag due to the presence of more electronegative sp^2 carbons. A smaller peak at 289 eV indicated the presence of the carbonyl carbon.[35,36] Another peak at 286 eV may have been due to the emission from carbon next to sulfur and the carbon

https://doi.org/10.1021/acsami.2c07610
ACS Appl. Mater. Interfaces 2022, 14, 38270−38280

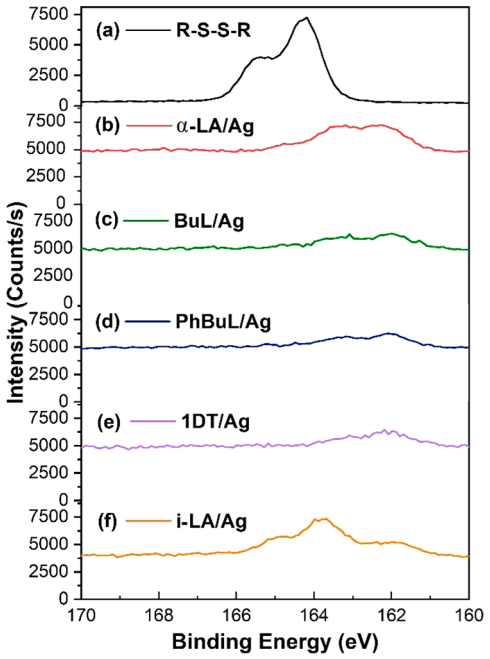

Figure 3. XPS S2p spectra of α-LA (a), α-LA/Ag (b), BuL/Ag (c), PhBuL/Ag (d), 1DT/Ag (e), and i-LA/Ag (f).

next to carbonyl groups.[37] The C1s for 1DT/Ag showed a peak at 285 eV characteristic of the 1DT chain length with 10 sp^3 carbons.[38]

The atomic ratio of carbon to Ag was obtained (Table S1) where the C/Ag ratio for α-LA/Ag was 2.40, BuL/Ag was 0.69, PhBuL/Ag was 0.96, i-LA/Ag was 0.57, and 1DT/Ag was 0.90. From this data, it was apparent that the C/Ag ratios did not correlate with the number of carbon atoms in each of the compounds used to obtain the SAMs. The α-LA compound with the lowest number of carbon atoms (eight) gave the highest C/Ag ratio, which indicated good coverage of the Ag by the SAM formed from α-LA. In contrast, BuL, with 12 carbon atoms, had the lowest C/Ag ratio, which suggested lower coverage. PhBuL with 18 carbon atoms also showed low coverage, while 1DT with 10 carbon atoms had relatively good coverage. Although all of the measurements were taken under the same conditions, adventitious carbon can contaminate the sample while conducting the experiment, and therefore the trend has to be interpreted cautiously. The coverage can also be explained by looking at the S/Ag ratio also where the values are 0.40 for α-LA/Ag, 0.18 for BuL/Ag, 0.21 for PhBuL/Ag, 0.14 for 1DT/Ag, and 0.34 for i-LA/Ag. Although a packing density similar to α-LA/Ag was expected for i-LA,[30] the C/Ag and S/Ag ratios of i-LA/Ag indicated that i-LA exhibited lower coverage than α-LA on Ag and existed in a partially bound form that was more disordered. Peak fitting analysis confirmed that the ratio of oxygen to sulfur was 1:1 in the case of α-LA, BuL, PhBuL, and i-LA, while no oxygen peak was observed for 1DT, indicating that the SAMs were not oxidized (Table S1). The stability of the silver surface and the question of whether the SAMs passivated it were investigated by looking at the $Ag3d_{5/2}$ doublet peak and O1s peaks. The Ag^0 peak occurs at 368.2 and 374.8 eV (Figure S15b). In the presence of Ag^+ or oxidized Ag, these peaks would occur at lower binding energies. XPS spectra of the bare Ag electrode, which was processed under the same conditions as the SAM-coated

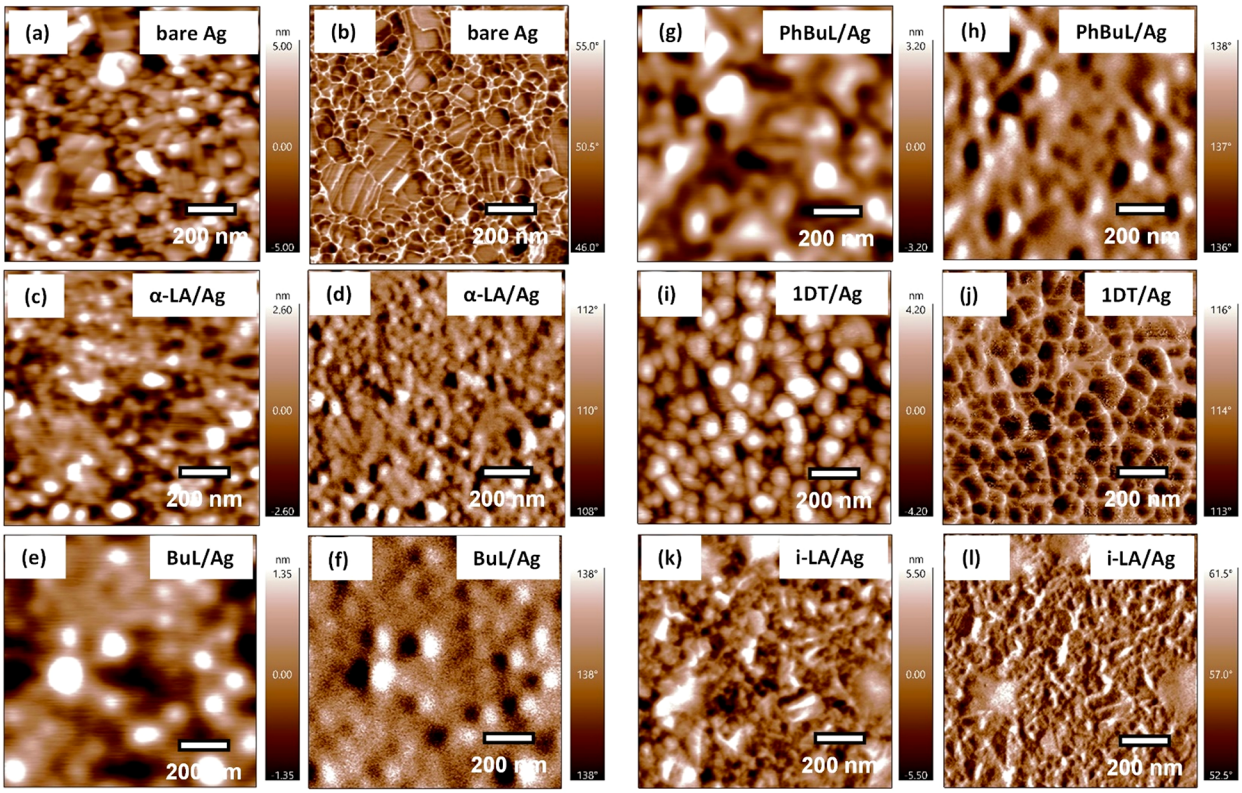

Figure 4. 1 μm × 1 μm AFM topography (left column) and phase images (right column): bare Ag (a, b); α-LA/Ag (c, d); BuL/Ag (e, f); PhBuL/Ag (g, h); 1DT/Ag (i, j); i-LA/Ag (k, l).

https://doi.org/10.1021/acsami.2c07610
ACS Appl. Mater. Interfaces 2022, 14, 38270−38280

electrode, showed a slight shift to lower energies in the Ag3d spectra compared to the Ag back electrodes with SAM, which indicated partial oxidation of the Ag surface.[38] These results suggest that the SAMs have a passivating effect on silver back electrodes which was corroborated by looking at the O1s core spectra where bare Ag was compared with that of SAMs/Ag. The bare Ag showed peaks at 531 V and above which showed the possibility of the presence of Ag_2CO_3. For SAMs/Ag, 1DT/Ag showed no peaks, but there are peaks at binding energies above 531 eV for α-LA/Ag, BuL/Ag, PhBuL/Ag, and i-LA/Ag, indicative of C−O and C═O bonds, while peaks indicating the presence of oxidized Ag (usually indicated by peaks at lower binding energies around ∼529 eV) were absent; in summary, it was apparent that the silver was stable in the presence of the SAM.[27,39]

3.2. Contact Angle Measurements. Contact angle measurements were performed by using a Rame-Hart 100-00 goniometer . The contact angle of a water drop was compared with the contact angles of each SAM on Ag. Water on a bare Ag surface gave a contact angle of 60°, and the contact angles of α-LA/Ag, BuL/Ag, PhBuL/Ag, 1DT/Ag, and i-LA/Ag on Ag were 79°, 81°, 84°, 84°, and 72°, respectively. The results show that all the SAMs make the surface more hydrophobic compared to bare Ag. α-LA and i-LA had the least impact on the contact angle due to the presence of the polar carbonyl group, while 1DT, BuL, and PhBuL, with less polar end groups, gave higher contact angles, making the Ag surface more hydrophobic.

3.3. Atomic Force Microscopy (AFM). AFM images give a qualitative measure of the coverage of the SAMs (Figure 4), topography images give information about the coverage and surface roughness, and phase images give information about the formation of domains. Upon comparison with bare Ag (Figure 4a), the lighter parts of the topography images of the SAM/Ag samples (Figure 4c,e,g,i) are domains formed by SAMs on the silver surface (the dark regions in the phase images (Figure 4d,f,h,j) are due to the dissipative nature of the phase mode).[13,40,41] The root-mean-square (RMS) roughness was calculated from the topography images, and it was found that bare Ag had an RMS roughness of 1.26 nm, which, on treatment with SAMs, changed to 1.64 nm for α-LA, 1.54 nm for BuL, 1.72 nm for PhBuL, 1.01 nm for 1DT, and 3.04 nm for i-LA/Ag. These changes can be taken as a measure of disorder due to the presence of SAMs.[42] Therefore, the low RMS roughness apparent for 1DT suggested very good coverage of the Ag and a high degree of order. In contrast, the increase in the RMS roughness for α-LA/Ag, BuL/Ag, PhBuL/Ag, and i-LA/Ag suggested a more disordered arrangement of these SAMs on Ag. The very high RMS roughness of i-LA/Ag compared to α-LA/Ag was consistent with the XPS results, which showed that the binding of i-LA molecules to the surface of Ag was partial.

3.4. UV Photoelectron Spectroscopy (UPS). To obtain further insight into the electronic properties of the SAM/Ag surfaces, UPS (Figures S17 and S18) was used to find the work function (Φ_b) of the Ag surface upon SAM/Ag formation and after deposition of the F8BT semiconducting polymer layer on top of the SAM/Ag (Table 1). We use F8BT films of 10−20 nm thickness on SAM/Ag for these measurements. The work function measurements through UPS give the minimum work function in a patchy nonuniform sample with a reported error of ±0.05 eV.[43] Valence band spectra of F8BT on Ag were also recorded to calculate the difference between the HOMO level of F8BT and the Fermi level of Ag, which gives the hole injection barrier (HIB) from Ag to the HOMO of F8BT. On the basis of the results, HIB decreased significantly for α-LA/Ag compared to all the other cases, which suggested lower contact resistance for SAMs formed from α-LA. i-LA/Ag also showed a slight increase in work function compared to bare Ag from 4.4 to 4.6. It is anticipated that in the presence of the SAM the positive charges from Ag are injected into the F8BT layers easily, because of a better electrical contact and/or a change in work function of Ag. Having two sulfur bonds instead of one led to a reduction of the contact resistance, as seen by the increase in current density with the α-LA/Ag. The tunneling of charges through the SAM, which depends on the bond length and the degree of disorder in the arrangement of the SAMs, may have also played a role in reducing the contact resistance. A look at the detailed electronic states of the SAM as well as the through-bond tunneling through the LUMO levels of the SAMs could confirm this.[44,45] The formation of SAMs on Ag is known to result in a strong Ag−S dipole, which induces a Fermi-level pinning that causes a significant shift in the HOMO of the adsorbed molecule.[46] The overall change in the work function is caused by the Ag−S bond dipole as well as the cosine component of molecular dipole (dependent on the orientation of the SAM molecule on the Ag surface) from the surface normal.[47] This causes a weak dependence of device performance on the work function of the metal surface. This can influence the tunneling attenuation factor and the contact resistance.[48] It has been previously reported that alkyl chains in the SAMs help with tunneling of holes into a p-type semiconductor if SAMs are chemically bound to the Ag surface (otherwise the molecules act as an insulating layer).[48,49]

Table 1. Work Function, Φ_b, and Hole Injection Barrier (HIB) of Ag Back Electrodes after Deposition of SAM and F8BT[a]

sample	Φ_b(SAM-Ag) (eV)[b]	Φ_b(F8BT/SAM/Ag) (eV)	$\Delta\Phi_b$ (eV)	HIB (eV)[c]
bare Ag	4.4	4.4	0	1.8
α-LA/Ag	4.8	4.6	−0.2	1.1
BuL/Ag	4.4	4.4	0	1.7
PhBuL/Ag	4.4	4.4	0	1.4
1DT/Ag	3.9	4.1	+0.2	1.6−1.7
i-LA/Ag	4.6	4.7	+0.1	1.4

[a]F8BT thickness: 10−20 nm. [b]Φ_b is the work function of Ag found through UPS. [c]HIB is the energy difference between Φ_b and HOMO of the F8BT polymer.

3.5. Current Density−Voltage (*J*−*V*) Measurements. To understand the effect of the SAM on the charge transport in the F8BT diodes, current density versus voltage (*J*−*V*) measurements of devices with and without the SAM layers (Figure 5a) were collected. The results show that the turn-on voltage was reduced from 0.22 ± 0.02 V for the bare Ag back electrode to 0.14 ± 0.025 V for α-LA/Ag, 0.21 ± 0.01 V for PhBuL/Ag, and 0.13 ± 0.17 for i-LA/Ag; however, the turn-on voltage increased for 1DT/Ag and BuL/Ag to 0.31 ± 0.01 and 0.33 ± 0.01, respectively (Figure 5a,b, Table 2, and Figures S19−S20). In addition, the current density also followed this trend. The current density at 2 V increased by more than a factor of 2 for PhBuL/Ag, α-LA/Ag, and i-LA/Ag compared to bare Ag where the *J* value was the highest for the case of i-LA/Ag, and the current density dropped by a factor of 2 for 1DT/

https://doi.org/10.1021/acsami.2c07610
ACS Appl. Mater. Interfaces 2022, 14, 38270−38280

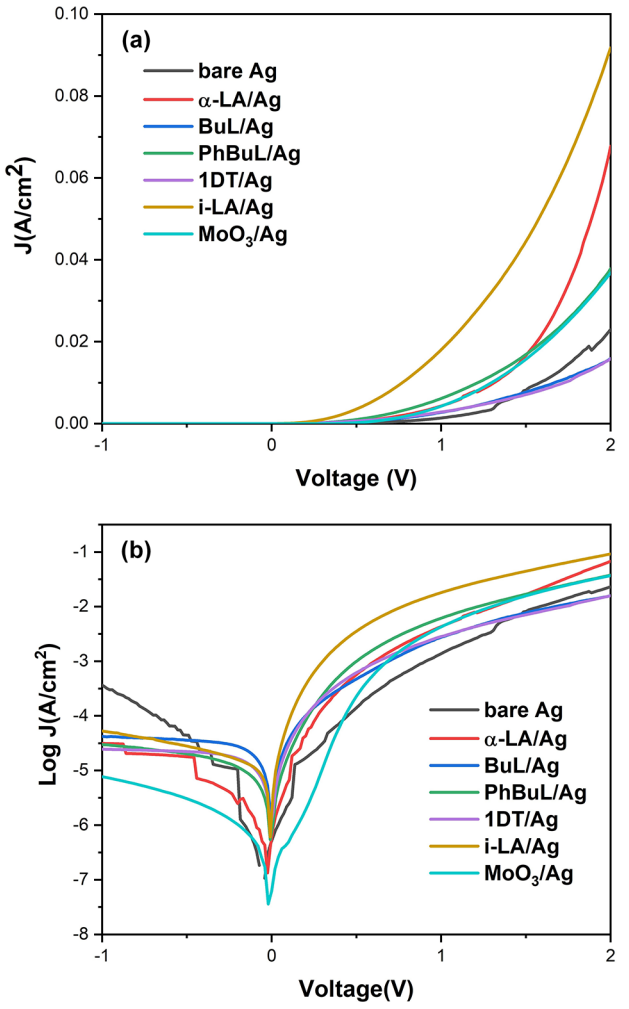

Figure 5. (a) Current density (J) versus voltage curves of F8BT devices with Ag as the back electrode without and with a SAM formed from α-LA, BuL, PhBuL, 1DT, i-LA, and MoO_3/Ag. (b) Log J versus voltage of the seven types of devices.

Ag and BuL/Ag (Table 2). Therefore, it was apparent that i-LA/Ag, α-LA, and PhBuL SAMs improve the electrical characteristics of the diodes.

3.6. Thickness Measurements and Raman Spectroscopy. The interaction of the SAM with the F8BT also affects the thickness of the F8BT layer.[50,28] Thickness measurements of the F8BT layer using a surface profilometer confirmed that the observed increase of current density in α-LA/Ag devices correlated to a reduced thickness of the F8BT film when spin-coated on α-LA/Ag. The F8BT thicknesses were 252 ± 8 nm for F8BT on bare silver, 196 ± 12 nm for F8BT on α-LA/Ag, 222 ± 16 nm for F8BT on BuL/Ag, 163 ± 21 nm for F8BT on PhBuL/Ag, 233 ± 9 nm for F8BT on 1DT/Ag, and 200.2 ± 4.9 nm for F8BT on i-LA/Ag. Series resistance is expected to be lower for thinner semiconducting films; hence, current density increases.[50−52] This was generally observed to be the case for the devices with α-LA/Ag, i-LA/Ag, and PhBuL/Ag, which showed high current density and caused thinner F8BT films. On normalizing the current density values with the thickness of F8BT, it was found that the trend observed for the electrical characteristics of the devices was the same before normalization. The changes in the orientation of the polymer were confirmed by Raman spectroscopy (Figure S15) where the dioctylfluorine (F8) ring stretching mode occurring at 1608 cm^{-1}, which is the electron-withdrawing group on F8BT, shifted slightly in the presence of the SAMs compared to the pristine F8BT film on Ag.[28,53,54] The Raman spectra for F8BT on i-LA and PhBuL SAMs shifted the most from 1608 cm^{-1}, which suggested more significant changes in the packing or orientation of the polymer chains of F8BT. Both the thickness measurements of F8BT and the AFM images that confirmed the degree of disorder and coverage supported the trends obtained with $J-V$ curves. This indicated which SAMs imparted a better electrical contact between the Ag and the semiconducting polymer. We also looked at the I_{1608}/I_{1547} ratio, which gives information about the torsional angle between F8-BT units, and hence, about the backbone planarity. The I_{1608}/I_{1547} ratio for F8BT on bare Ag was 1.06, α-LA/Ag was 0.97, BuL/Ag was 0.95, PhBuL/Ag was 0.96, 1DT/Ag was 0.97, and i-LA/Ag was 1.06. The increase in this relative intensity corresponds to increasing backbone planarity.[55] We also thinned down the F8BT films by using diluted solutions of 20 mg/mL (see Figure S16). We spin-coated F8BT from 5 times, 10 times, and 20 times diluted solutions and looked at the F8 and BT signals. α-LA/Ag, i-LA/Ag, and PhBuL/Ag showed the best signals for the thinner F8BT films, which indicated that the SAMs helped the polymer to achieve the lowest energy conformation during the spin-coating process.

The reason for the poor performance of BuL compared to the α-LA could be the effect of the orientation of the molecule influenced by the chain length as well as the structure of the end groups. In 2006, Weiss and co-workers reported the use of scanning tunneling microscopy (STM) to study the effect of molecular orientation of the n-alkanethiol SAMs on the electrical behavior of the metal electrodes in large-area molecular junctions.[56] The conductance through the SAMs

Table 2. $J-V$ Characteristics of the Inverted F8BT Diodes Fabricated with SAMs/Ag[a]

sample	n values	current density at 2 V (mA/cm^2)	turn-on voltage (V)	barrier height (eV)	normalized current density[b] (mA/cm^2)
bare Ag	1.6	15 ± 2.4	0.22 ± 0.02	0.71 ± 0.02	15 ± 2.4
α-LA/Ag	3.5	68 ± 1.4	0.14 ± 0.03	0.63 ± 0.02	52 ± 1.8
BuL/Ag	4.6	16 ± 1.6	0.31 ± 0.01	0.74 ± 0.02	14 ± 7.7
PhBuL/Ag	4.8	38 ± 7.7	0.21 ± 0.01	0.69 ± 0.03	24 ± 1.4
1DT/Ag	4.8	16 ± 1.6	0.33 ± 0.02	0.76 ± 0.04	14 ± 6.9
i-LA/Ag	2.9	89 ± 1.1	0.13 ± 0.02	0.64 ± 0.04	70 ± 1.6
MoO_3/Ag	6.8	37 ± 5.5	0.20 ± 0.03	0.74 ± 0.05	-

[a]The error in the values listed below is determined by taking the standard deviation of the values obtained from analysis of ten different devices for each sample type. The large error is caused by the large error obtained from thickness measurements. [b]Normalized current density was calculated by multiplying current density at 2 V by the ratio of F8BT thickness on SAM/Ag to that on bare Ag.

https://doi.org/10.1021/acsami.2c07610
ACS Appl. Mater. Interfaces 2022, 14, 38270−38280

of lipoic acid derivatives on Ag is independent of temperature, whereas it is largely dependent on the length of the SAM molecule or the thickness of the monolayer.[57−59] This establishes that the electrical transport mechanism is non-resonant through-bond tunneling. Other factors affecting the conductance are the binding energy, chain length, and number of sulfur atom bonds to the Ag metal. With the help of large-area molecular junctions, the contact resistance was found to vary linearly with the number of carbon atoms,[60] where the contact resistance (R_0) is given by $R_0 = R_0 \exp(\beta n)$, where R is the total resistance, n gives the number of carbon atoms, and β is the structure-dependent attenuation factor.[59,61] It is notable that the SAM of i-LA showed the best electrical behavior despite not altering the work function of the Ag as much as α-LA did, and PhBuL showed the third best device performance despite not altering the work function at all. A possible explanation of this result can be because of the lowering of series resistance due to thinner F8BT films in the presence of PhBuL. This could be attributed to the PhBuL/Ag surface being the most hydrophobic due to the presence of the phenyl group. The contact resistance is expected to increase with the chain length, while the end phenyl groups can provide favorable electronic interactions with the F8BT conjugated polymer that counter the increase in resistance. Thus, PhBuL proved to be a better SAM than BuL in this study in terms of device performance.

3.7. Barrier Height (Φ_h) Measurements. The barrier height between the Fermi level of Ag and the HOMO of F8BT can be found from the equation for current density for Schottky barrier diodes:[46,62,63]

$$I = AA^*T^2 \exp\left(-\frac{q\Phi_h}{KT}\right)\left[\exp\left(\frac{qV}{nKT}\right) - 1\right] \quad (1)$$

where A is the diode area, A^* is 120 A/(cm^2 K^2) which is the Richardson constant for organic polymers,[64] q is the electronic charge, Φ_h is the effective barrier height, K is Boltzmann's constant, T is room temperature, V is the voltage at which the current is measured, and n is the ideality factor which is given by the slope of a fit to the semilogarithmic $J-V$ curve. n is calculated as follows:[63]

$$n = \left(\frac{q}{KT}\frac{dV}{d(\ln I)}\right) \quad (2)$$

The ideality factor n for the different devices was found to be 1.6 for bare Ag, 3.5 for α-LA/Ag, 4.6 for BuL/Ag, 4.8 for PhBuL/Ag, 4.8 for 1DT/Ag, 2.9 for i-LA/Ag, and 6.8 for MoO_3/Ag. The n values are all greater than 1, which could be attributed to a number of reasons such as organic layer effects or the inhomogeneities in the organic layer. Interfacial effects and the presence of any AgO_x can also lead to increased values of n.[27] The barrier heights obtained by analyzing the $J-V$ curves using eqs 1 and 2 are shown in Table 2. This behavior only considers the space-charge-limited current (SCLC) regime, which is the behavior of the device above the turn-on voltage. The log V versus Log J curves should ideally give a slope of 2 in this region (see Figure S22). The slopes for the different types of devices in the SCLC region according to the Mott−Gurney rule (Table 3) are 2.8 for bare Ag, 2.9 for α-LA/Ag, 2.5 for BuL/Ag, 2.7 for PhBuL/Ag, 2.2 for 1DT/Ag, 2.4 for i-LA/Ag, and 3.4 for MoO_3/Ag. The slope deviates slightly from the ideal value for the SAM/Ag devices, but most SAM/Ag devices improve upon the bare Ag and MoO_3/Ag devices.

Table 3. Results from SCLC Analysis Obtained from the $J-V$ Curves

sample	slope	mobility μ (cm^2/(V s))
bare Ag	2.8	3.5×10^{-4}
α-LA/Ag	2.9	4.6×10^{-4}
BuL/Ag	2.5	3.1×10^{-4}
PhBuL/Ag	2.7	9.1×10^{-4}
1DT/Ag	2.4	3.4×10^{-4}
i-LA/Ag	3.4	2.4×10^{-4}

The presence of oxides at the interface can cause the slope to vary from 2, which is seen in the case of MoO_3/Ag and bare Ag substrates where the silver surface has oxidized. While in the presence of SAMs, tunneling of charges at the interface is a possibility that also causes the slope to deviate. The equation for mobility according to this rule is given as follows:

$$J = \frac{9\varepsilon\varepsilon_0\mu V^2}{8L^3} \quad (3)$$

In eq 3, ε is the dielectric constant of F8BT which is 3.5,[63] ε_0 is the permittivity of free space, μ is the hole mobility, L is the thickness of the active layer, and J and V are the current density and voltage from the $J-V$ curves, respectively. The F8BT hole mobilities for the devices were found to be as follows: 3.5×10^{-4} cm^2/(V s) for bare Ag, 4.6×10^{-4} cm^2/(V s) for α-LA/Ag, 3.1×10^{-4} cm^2/(V s) for BuL/Ag, 9.1×10^{-4} cm^2/(V s) for PhBuL/Ag, 3.4×10^{-4} cm^2/(V s) for 1DT/Ag, and 2.4×10^{-4} cm^2/(V s) for i-LA/Ag. The F8BT hole mobility has been reported previously to be in the range of $10^{-6}-10^{-3}$ cm^2/(V s) depending whether the mobility is found through the SCLC or the OFET method.[65−67] It is apparent from the ideality factor and the Mott−Gurney law that the devices have inhomogeneity in the active layer, and possible tunneling occurs through the metal−polymer interface due to the SAMs.

Despite these variations, it is apparent from the $J-V$ curve data and UPS result that i-LA and α-LA showed the best performance in terms of lowering the work function of Ag, reducing the barrier height and turn-on voltage, and giving the largest current.

3.8. Infrared Reflective Absorption Spectroscopy Measurements. To obtain molecular-level insight into the interaction of the α-LA and i-LA SAMs with the F8BT polymer and on the orientation of the SAMs on the silver surface, we acquired FT-IRRAS measurements of α-LA/Ag and F8BT/α-LA/Ag as well as i-LA/Ag and F8BT/i-LA/Ag samples (Figure S23). The similar intensities of the methylene C−H stretch modes of the i-LA/Ag and α-LA/Ag samples, shown in Figure S23a, confirm that the loading density of the two lipoic acid layers is about the same. The most informative aspects regarding the interaction of the lipoic acid layer with the F8BT polymer are the values of C═O stretch bands of the carboxyl groups, shown in Figures S23b and S23c. The C═O stretch of the CO_2H group of α-LA/Ag prior to depositing F8BT, shown in Figure S23b, trace (1), features main peaks at 1727 and 1658 cm^{-1}. The 1727 cm^{-1} band is typical for weak carboxyl C═O interaction with alkyl moieties such as CH_2 groups of neighboring α-LA.[68] The substantial red-shift of the 1658 cm^{-1} band points to H-bonding interaction with the OH group of an adjacent α-LA molecule, possibly including the $(CO_2H)_2$ dimer structure.[68] Upon deposition of F8BT onto the α-LA SAM, a band grows in at 1709 cm^{-1} at the expense of

https://doi.org/10.1021/acsami.2c07610
ACS Appl. Mater. Interfaces 2022, 14, 38270−38280

decreasing 1658 and 1727 cm^{-1} peaks (Figure S23b, trace (2)). The close to 20 cm^{-1} red-shift compared to the 1727 cm^{-1} band is consistent with interaction with aromatic moieties of the polymer.[69] Taken together, these observations indicate that deposition of the F8BT results in substantial reorientation of the α-LA carboxyl end group toward interaction with the polymer.

For i-LA, the intense sharp C═O stretch observed at 1740 cm^{-1} is characteristic for free CO_2H groups that do not interact with neighboring molecules (Figure S23c, trace (1)).[70] The difference with α-LA SAM, which does not exhibit bands of free CO_2H, can be rationalized by the close to vertical orientation of the C−C bond attached to the dithiolanyl ring of i-LA for bidentate S−S anchoring of the Ag surface (Figure 1). By contrast, the alkyl chain of α-LA is expected to be tilted assuming bidentate anchoring of the dithiolanyl ring, rendering the CO_2H terminus prone to interaction with neighboring lipoic acid molecules. Furthermore, the high intensity of the 1740 cm^{-1} band suggests perpendicular orientation of the C═O group (FT-IRRAS exclusively records p components of vibrational modes). As shown in Figure S23c, trace (2), the free CO_2H groups of i-LA almost quantitatively engage in interactions with the polymer upon F8BT deposition, as indicated by the 1709 cm^{-1} shoulder, as well as neighboring i-LA methylene moieties according to the growth at 1727 cm^{-1}.

From these FT-IRRAS measurements it is apparent that the i-LA is oriented more out-of-plane compared to α-LA, which is consistent with their molecular structure. On coating the α-LA/Ag and i-LA/Ag samples with F8BT, the orientations of both SAMs are altered, indicating that intermolecular interactions are occurring. Further studies of different infrared active bands in the SAM/Ag system are planned to obtain a more complete picture of the nature of the SAM/F8BT interactions.

4. CONCLUSIONS

Self-assembled monolayers (SAMs) of (±)-α-lipoic acid (α-LA), (±)-butyl 5-(1,2-dithiolan-3-yl)pentanoate (BuL), (±)-4-phenylbutyl 5-(1,2-dithiolan-3-yl)pentanoate (PhBuL), 1-decanethiol (1DT), and isolipoic acid (i-LA) on Ag electrodes were used to fabricate inverted F8BT diodes for the purpose of passivating the Ag surface as well as reducing the contact resistance between Ag and the F8BT conjugated polymer. The binding of the SAMs on the Ag surface was probed by X-ray photoelectron spectroscopy, and the SAM/Ag morphology was studied by using atomic force microscopy. Current−voltage measurements were conducted to study the electronic behavior of the devices and determine work function and barrier heights. It was found that SAMs formed by α-LA, i-LA, and PhBuL on Ag lowered the hole injection barrier and/or altered the work function of the Ag back electrode. We attribute this result to better charge injection from the Ag electrode to the F8BT due to a lowering of the hole-injection barrier. Because LA derivatives are amenable to many synthetic modifications, this is potentially a versatile method for engineering the morphological and electrical properties of metal−polymer interfaces in inverted organic electronic devices.

■ ASSOCIATED CONTENT

Supporting Information

The Supporting Information is available free of charge at https://pubs.acs.org/doi/10.1021/acsami.2c07610.

Schematic of synthesis of i-LA; ^1H NMR and ^{13}C NMR spectra of BuL, PhBuL, diethyl 2-(hex-5-en-1-yl)-malonate, 2-(hex-5-en-1-yl)propane-1,3-diol, 2-(hex-5-en-1-yl)propane-1,3-diyl dimethanesulfonate, 7-((methylsulfonyl)oxy)-6-(((methylsulfonyl)oxy)methyl) heptanoic acid, i-LA; UPS spectra and expanded UPS spectra of SAM/Ag and F8BT/SAM/Ag; *J*−*V* and Log *J*−*V* curves of 10 inverted hole-only devices; average *J*−*V* of 10 devices at 2 V and normalized *J*−*V*, turn-of-voltage and barrier height; Log *V* versus Log *J* curves; FT-IRRAS spectra of SAM-F8BT layers (PDF)

■ AUTHOR INFORMATION

Corresponding Authors

Elena Galoppini − *Department of Chemistry, Rutgers University, Newark, New Jersey 07102, United States;* orcid.org/0000-0003-0833-7436; Email: galoppin@newark.rutgers.edu

Deirdre M. O'Carroll − *Department of Chemistry and Chemical Biology, Rutgers University, Piscataway, New Jersey 08854, United States; Department of Materials Science and Engineering, Rutgers University, Piscataway, New Jersey 08854, United States;* orcid.org/0000-0001-7209-4278; Email: ocarroll@rutgers.edu

Authors

Sneha Sreekumar − *Department of Chemistry and Chemical Biology, Rutgers University, Piscataway, New Jersey 08854, United States*

Marzieh Heidari − *Department of Chemistry, Rutgers University, Newark, New Jersey 07102, United States*

Zhongkai Cheng − *Department of Chemistry and Chemical Biology, Rutgers University, Piscataway, New Jersey 08854, United States*

Hemanth Maddali − *Department of Chemistry and Chemical Biology, Rutgers University, Piscataway, New Jersey 08854, United States*

Krystal House − *Department of Chemistry and Chemical Biology, Rutgers University, Piscataway, New Jersey 08854, United States*

Heinz Frei − *Molecular Biophysics and Integrated Bioimaging Division, Lawrence Berkeley National Laboratory, University of California, Berkeley, Berkeley, California 94720, United States;* orcid.org/0000-0001-8755-6367

Complete contact information is available at: https://pubs.acs.org/10.1021/acsami.2c07610

Author Contributions

S.S and M.H. contributed equally to this work; D.M.O. and E.G. conceived the original idea and developed the experimental plans with help from S.S. and M.H.; S.S. performed the experiments and analyses for the binding studies (Raman spectroscopy, XPS) and the electrical and electronic behavior (UPS and *I*−*V* measurements); M.H. synthesized the BuL, PhBuL, and i-LA compounds and performed the mass spectrometry, FT-IR, and NMR analyses for the synthesized compounds; the AFM data acquisition and analysis were performed by H.M. and K.H.; the F8BT thickness measurements were conducted by Z.C.; Z.C. assisted with the hole-only devices design and testing; H.F. performed the FT-IRRAS measurements and aided in analysis and interpretation of the data; the manuscript was written by

https://doi.org/10.1021/acsami.2c07610
ACS Appl. Mater. Interfaces 2022, 14, 38270−38280

S.S., D.M.O, M.H., and E.G.; H.M., Z.C., K.H., and H.F. assisted with editing the relevant parts of the manuscript; all authors agreed to the final version of the manuscript and agree to be accountable for the content within.

Notes

The authors declare no competing financial interest.

■ ACKNOWLEDGMENTS

The authors are grateful to Prof. Sylvie Rangan and Jonathan Viereck for their assistance with Ultraviolet Photoelectron Spectroscopy and X-ray Photoelectron Spectroscopy. This work was supported in part by the National Science Foundation (NSF) under Grants DMR-1552954 (D.M.O.) and CHE-1904654 (E.G.). This work was also supported in part by the Director, Office of Science, Office of Basic Energy Sciences, Division of Chemical, Geological and Biosciences of the US Department of Energy, under Contract DE-AC02-05CH11231.

■ REFERENCES

(1) Walzer, K.; Maennig, B.; Pfeiffer, M.; Leo, K. Highly Efficient Organic Devices Based on Electrically Doped Transport Layers. *Chem. Rev.* **2007**, *107*, 1233−1271.

(2) Forrest, S. R. Ultrathin Organic Films Grown by Organic Molecular Beam Deposition and Related Techniques. *Chem. Rev.* **1997**, *97*, 1793−1896.

(3) Hung, L.; Chen, C. Recent Progress of Molecular Organic Electroluminescent Materials and Devices. *Mater. Sci. Eng., R* **2002**, *39*, 143−222.

(4) Kelley, T. W.; Baude, P. F.; Gerlach, C.; Ender, D. E.; Muyres, D.; Haase, M. A.; Vogel, D. E.; Theiss, S. D. Recent Progress in Organic Electronics: Materials, Devices, and Processes. *Chem. Mater.* **2004**, *16*, 4413−4422.

(5) Myers, J. D.; Xue, J. Organic Semiconductors and their Applications in Photovoltaic Devices. *Polym. Rev.* **2012**, *52*, 1−37.

(6) Root, S. E.; Savagatrup, S.; Printz, A. D.; Rodriquez, D.; Lipomi, D. J. Mechanical Properties of Organic Semiconductors for Stretchable, Highly Flexible, and Mechanically Robust Electronics. *Chem. Rev.* **2017**, *117*, 6467−6499.

(7) Tang, C. W.; VanSlyke, S. A. Organic Electroluminescent Diodes. *Appl. Phys. Lett.* **1987**, *51*, 913−915.

(8) Kim, D. Y.; Subbiah, J.; Sarasqueta, G.; So, F.; Ding, H.; Irfan; Gao, Y. The Effect of Molybdenum Oxide Interlayer on Organic Photovoltaic Cells. *Appl. Phys. Lett.* **2009**, *95*, 093304.

(9) Liang, Z.; Zhang, Q.; Jiang, L.; Cao, G. ZnO Cathode Buffer Layers for Inverted Polymer Solar Cells. *Energy Environ. Sci.* **2015**, *8*, 3442−3476.

(10) Po, R.; Carbonera, C.; Bernardi, A.; Camaioni, N. The Role of Buffer Layers in Polymer Solar Cells. *Energy Environ. Sci.* **2011**, *4*, 285−310.

(11) Dou, L.; You, J.; Yang, J.; Chen, C.-C.; He, Y.; Murase, S.; Moriarty, T.; Emery, K.; Li, G.; Yang, Y. Tandem Polymer Solar Cells Featuring a Spectrally Matched Low-bandgap Polymer. *Nat. Photonics* **2012**, *6*, 180−185.

(12) Li, G.; Chang, W.-H.; Yang, Y. Low-bandgap Conjugated Polymers Enabling Solution-Processable Tandem Solar Cells. *Nat. Rev. Mater.* **2017**, *2*, 17043.

(13) Liu, Y.; Qiu, X.; Soni, S.; Chiechi, R. C. Charge Transport Through Molecular Ensembles: Recent progress in Molecular Electronics. *Chem. Phys. Rev.* **2021**, *2*, 021303.

(14) You, J.; Dou, L.; Yoshimura, K.; Kato, T.; Ohya, K.; Moriarty, T.; Emery, K.; Chen, C.-C.; Gao, J.; Li, G.; Yang, Y. A Polymer Tandem Solar Cell with 10.6% Power Conversion Efficiency. *Nat. Commun.* **2013**, *4*, 1446.

(15) Sha, W. E. I.; Li, X.; Choy, W. C. H. Breaking the Space Charge Limit in Organic Solar Cells by a Novel Plasmonic-Electrical Concept. *Sci. Rep.* **2015**, *4*, 6236.

(16) Choy, W. C. H. The Emerging Multiple Metal Nanostructures for Enhancing the Light Trapping of Thin film Organic Photovoltaic Cells. *Chem. Commun.* **2014**, *50*, 11984−11993.

(17) Nomura, K.; Ohta, H.; Takagi, A.; Kamiya, T.; Hirano, M.; Hosono, H. Room-Temperature Fabrication of Transparent Flexible Thin-Film Transistors using Amorphous Oxide Semiconductors. *Nature* **2004**, *432*, 488−492.

(18) Hosono, H.; Kim, J.; Toda, Y.; Kamiya, T.; Watanabe, S. Transparent Amorphous Oxide Semiconductors for Organic Electronics: Application to Inverted OLEDs. *Proc. Natl. Acad. of Sci.* **2017**, *114*, 233−238.

(19) Roh, J.; Lee, T.; Kang, C.-m.; Kwak, J.; Lang, P.; Horowitz, G.; Kim, H.; Lee, C. Injection-Modulated Polarity Conversion by Charge Carrier Density Control via a Self-Assembled Monolayer for All-Solution-Processed Organic Field-Effect Transistors. *Sci. Rep.* **2017**, *7*, 46365.

(20) Li, Y. Q.; Tang, J. X.; Xie, Z. Y.; Hung, L. S.; Lau, S. S. An Efficient Organic Light-Emitting Diode with Silver Electrodes. *Chem. Phys. Lett.* **2004**, *386*, 128−131.

(21) Jiang, P.; Liu, Z.-F.; Cai, S.-M. Growing Monodispersed PbS Nanoparticles on Self-Assembled Monolayers of 11-Mercaptoundecanoic Acid on Au(111) Substrate. *Langmuir* **2002**, *18*, 4495−4499.

(22) O'Carroll, D. M.; Petoukhoff, C. E.; Kohl, J.; Yu, B.; Carter, C. M.; Goodman, S. Conjugated Polymer-based Photonic Nanostructures. *Polym. Chem.* **2013**, *4*, 5181−5196.

(23) Mendoza, S. M.; Arfaoui, I.; Zanarini, S.; Paolucci, F.; Rudolf, P. Improvements in the Characterization of the Crystalline Structure of Acid-Terminated Alkanethiol Self-Assembled Monolayers on Au(111). *Langmuir* **2007**, *23*, 582−588.

(24) Casalini, S.; Bortolotti, C. A.; Leonardi, F.; Biscarini, F. Self-Assembled Monolayers in Organic electronics. *Chem. Soc. Rev.* **2017**, *46*, 40−71.

(25) Escoubas, L.; Carlberg, M.; Le Rouzo, J.; Pourcin, F.; Ackermann, J.; Margeat, O.; Reynaud, C.; Duche, D.; Simon, J.-J.; Sauvage, R.-M.; Berginc, G. Design and Realization of Light Absorbers using Plasmonic Nanoparticles. *Prog. Quantum Electron.* **2019**, *63*, 1−22.

(26) Liu, W.; Fang, Y.; Li, J. Copper Iodide Based Hybrid Phosphors for Energy-Efficient General Lighting Technologies. *Adv. Funct. Mater.* **2018**, *28*, 1705593.

(27) Cheng, Z.; Wang, Y.; O'Carroll, D. M. Influence of Partially-Oxidized Silver Back Electrodes on the Electrical Properties and Stability of Organic Semiconductor Diodes. *Org. Electron.* **2019**, *70*, 179−185.

(28) Cheng, X.; Noh, Y.-Y.; Wang, J.; Tello, M.; Frisch, J.; Blum, R.-P.; Vollmer, A.; Rabe, J. P.; Koch, N.; Sirringhaus, H. Controlling Electron and Hole Charge Injection in Ambipolar Organic Field-Effect Transistors by Self-Assembled Monolayers. *Adv. Funct. Mater.* **2009**, *19*, 2407−2415.

(29) Kim, C.-H.; Hlaing, H.; Hong, J.-A.; Kim, J.-H.; Park, Y.; Payne, M. M.; Anthony, J. E.; Bonnassieux, Y.; Horowitz, G.; Kymissis, I. Decoupling the Effects of Self-Assembled Monolayers on Gold, Silver, and Copper Organic Transistor Contacts. *Adv. Mater. Interfaces* **2015**, *2*, 1400384.

(30) Joly, K.; Mirri, G.; Willener, Y.; Horswell, S.; Moody, C.; Tucker, J. Synthesis of an Achiral Isomer of Lipoic Acid as an Anchor Group for SAM Formation on Gold Surfaces. *J. Org. Chem.* **2010**, *75*, 2395−8.

(31) Wilkop, T.; Xu, D.; Cheng, Q. Electrochemical Characterization of Pore Formation by Bacterial Protein Toxins on Hybrid Supported Membranes. *Langmuir* **2008**, *24*, 5615−5621.

(32) Tarlov, M. J.; Burgess, D. R. F.; Gillen, G. UV Photopatterning of Alkanethiolate Monolayers Self-Assembled on Gold and Silver. *J. Am. Chem. Soc.* **1993**, *115*, 5305−5306.

(33) Bandyopadhyay, S.; Chattopadhyay, S.; Dey, A. The Protonation State of Thiols in Self-Assembled Monolayers on Roughened Ag/Au Surfaces and Nanoparticles. *Phys. Chem. Chem. Phys.* **2015**, *17*, 24866−24873.

https://doi.org/10.1021/acsami.2c07610
ACS Appl. Mater. Interfaces 2022, 14, 38270−38280

(34) Hagenström, H.; Esplandiú, M. J.; Kolb, D. M. Functionalized Self-Assembled Alkanethiol Monolayers on Au(111) Electrodes: 2. Silver Electrodeposition. *Langmuir* **2001**, *17*, 839−848.
(35) Sauter, E.; Gilbert, C.-O.; Boismenu-Lavoie, J.; Morin, J.-F.; Zharnikov, M. Mixed Aliphatic Self-Assembled Monolayers with Embedded Polar Group. *J. Phys. Chem. C* **2017**, *121*, 23017−23024.
(36) Ishida, T.; Mizutani, W.; Tokumoto, H.; Choi, N.; Akiba, U.; Fujihira, M. Insertion Process and Electrical Conduction of Conjugated Molecules in n-Alkanethiol Self-Assembled Monolayers on Au(111). *J. Vac. Sci. Technol. A* **2000**, *18*, 1437−1442.
(37) Esplandiu, M. J.; Noeske, P. L. M. XPS Investigations on the Interactions of 1,6-Hexanedithiol/Au(1 1 1) Layers with Metallic and Ionic Silver Species. *Appl. Surf. Sci.* **2002**, *199*, 166−182.
(38) Hutt, D. A.; Cooper, E.; Leggett, G. J. Structure and Mechanism of Photooxidation of Self-assembled Monolayers of Alkylthiols on Silver Studied by XPS and Static SIMS. *J. Phys. Chem. B* **1998**, *102*, 174−184.
(39) Petoukhoff, C.; Antonick, C.; Mariserla, B. M. K.; Dani, K.; O'Carroll, D. Oxidation of Planar and Plasmonic Ag Surfaces by Exposure to O2/Ar Plasma for Organic Optoelectronic Applications. *MRS Adv.* **2016**, *1*, 943.
(40) Kosaka, P. M.; González, S.; Domínguez, C. M.; Cebollada, A.; San Paulo, A.; Calleja, M.; Tamayo, J. Atomic force microscopy Reveals Two Phases in Single Stranded DNA Self-assembled Monolayers. *Nanoscale* **2013**, *5*, 7425−7432.
(41) Hajisalem, G.; Min, Q.; Gelfand, R.; Gordon, R. Effect of Surface Roughness on Self-Assembled Monolayer Plasmonic Ruler in Nonlocal Regime. *Opt. Express* **2014**, *22*, 9604−9610.
(42) Maddali, H.; House, K. L.; Emge, T. J.; O'Carroll, D. M. Identification of the Local Electrical Properties of Crystalline and Amorphous Domains in Electrochemically Doped Conjugated Polymer Thin Films. *RSC Adv.* **2020**, *10*, 21454−21463.
(43) Helander, M. G.; Greiner, M. T.; Wang, Z. B.; Lu, Z. H. Pitfalls in Measuring Work Function using Photoelectron Spectroscopy. *Appl. Surf. Sci.* **2010**, *256*, 2602−2605.
(44) Xie, Z.; Bâldea, I.; Frisbie, C. D. Energy Level Alignment in Molecular Tunnel Junctions by Transport and Spectroscopy: Self-Consistency for the Case of Alkyl Thiols and Dithiols on Ag, Au, and Pt Electrodes. *J. Am. Chem. Soc.* **2019**, *141*, 18182−18192.
(45) Xie, Z.; Bâldea, I.; Frisbie, C. D. Determination of Energy-Level Alignment in Molecular Tunnel Junctions by Transport and Spectroscopy: Self-Consistency for the Case of Oligophenylene Thiols and Dithiols on Ag, Au, and Pt Electrodes. *J. Am. Chem. Soc.* **2019**, *141*, 3670−3681.
(46) Tung, R. T. Electron transport at metal-semiconductor interfaces: General theory. *Phys. Rev. B* **1992**, *45*, 13509−13523.
(47) Lindell, L.; Çakır, D.; Brocks, G.; Fahlman, M.; Braun, S. Role of Intrinsic Molecular Dipole in Energy Level Alignment at Organic Interfaces. *Appl. Phys. Lett.* **2013**, *102*, 223301.
(48) Gwinner, M. C.; Khodabakhsh, S.; Giessen, H.; Sirringhaus, H. Simultaneous Optimization of Light Gain and Charge Transport in Ambipolar Light-Emitting Polymer Field-Effect Transistors. *Chem. Mater.* **2009**, *21*, 4425−4433.
(49) Haick, H.; Ambrico, M.; Ligonzo, T.; Tung, R. T.; Cahen, D. Controlling Semiconductor/Metal Junction Barriers by Incomplete, Nonideal Molecular Monolayers. *J. Am. Chem. Soc.* **2006**, *128*, 6854−6869.
(50) Braun, S.; de Jong, M. P.; Osikowicz, W.; Salaneck, W. R. Influence of the Electrode Work Function on the Energy Level Alignment at Organic-Organic Interfaces. *Appl. Phys. Lett.* **2007**, *91*, 202108.
(51) Güllü, Ö.; Türüt, A. Electrical Analysis of Organic Interlayer Based Metal/Interlayer/Semiconductor Diode Structures. *J. Appl. Phys.* **2009**, *106*, 103717.
(52) Liu, D.; Miao, Q. Recent Progress in Interface Engineering of Organic Thin film Transistors with Self-Assembled Monolayers. *Mater. Chem. Front.* **2018**, *2*, 11−21.
(53) Zaumseil, J.; McNeill, C. R.; Bird, M.; Smith, D. L.; Ruden, P. P.; Roberts, M.; McKiernan, M. J.; Friend, R. H.; Sirringhaus, H. Quantum efficiency of Ambipolar Light-Emitting Polymer Field-Effect Transistors. *J. Appl. Phys.* **2008**, *103*, 064517.
(54) Monson, T. C.; Lloyd, M. T.; Olson, D. C.; Lee, Y.-J.; Hsu, J. W. P. Photocurrent Enhancement in Polythiophene- and Alkanethiol-Modified ZnO Solar Cells. *Adv. Mater.* **2008**, *20*, 4755−4759.
(55) Schmidtke, J. P.; Kim, J.-S.; Gierschner, J.; Silva, C.; Friend, R. H. Optical Spectroscopy of a Polyfluorene Copolymer at High Pressure: Intra- and Intermolecular Interactions. *Phys. Rev. Lett.* **2007**, *99*, 167401.
(56) Moore, A. M.; Dameron, A. A.; Mantooth, B. A.; Smith, R. K.; Fuchs, D. J.; Ciszek, J. W.; Maya, F.; Yao, Y.; Tour, J. M.; Weiss, P. S. Molecular Engineering and Measurements to Test Hypothesized Mechanisms in Single Molecule Conductance Switching. *J. Am. Chem. Soc.* **2006**, *128*, 1959−1967.
(57) Tao, N. J. Electron transport in molecular junctions. *Nat. Nanotechnol.* **2006**, *1*, 173−181.
(58) Akkerman, H. B.; Blom, P. W.; de Leeuw, D. M.; de Boer, B. Towards Molecular Electronics with Large-Area Molecular Junctions. *Nature* **2006**, *441*, 69−72.
(59) Akkerman, H. B.; de Boer, B. Electrical Conduction through Single Molecules and Self-Assembled Monolayers. *J. Phys.: Condens. Matter.* **2007**, *20*, 013001.
(60) Akkerman, H. B.; Kronemeijer, A. J.; van Hal, P. A.; de Leeuw, D. M.; Blom, P. W. M.; de Boer, B. Self-Assembled-Monolayer Formation of Long Alkanedithiols in Molecular Junctions. *Small* **2008**, *4*, 100−104.
(61) Kronemeijer, A. J.; Huisman, E. H.; Akkerman, H. B.; Goossens, A. M.; Katsouras, I.; van Hal, P. A.; Geuns, T. C. T.; van der Molen, S. J.; Blom, P. W. M.; de Leeuw, D. M. Electrical Characteristics of Conjugated Self-Assembled Monolayers in Large-Area Molecular Junctions. *Appl. Phys. Lett.* **2010**, *97*, 173302.
(62) Petoukhoff, C. E.; Vijapurapu, D. K.; O'Carroll, D. M. Computational Comparison of Conventional and Inverted Organic Photovoltaic Performance Parameters with Varying Metal Electrode Surface Workfunction. *Sol. Energy Mater. Sol. Cells* **2014**, *120*, 572−583.
(63) Güllü, Ö.; Aydoğan, Ş.; Türüt, A. Fabrication and Electrical Characteristics of Schottky diode Based on Organic Material. *Microelectron. Eng.* **2008**, *85*, 1647−1651.
(64) Abthagir, P. S.; Saraswathi, R. Junction Properties of Metal/Polypyrrole Schottky Barriers. *J. Appl. Polym. Sci.* **2001**, *81*, 2127−2135.
(65) Zhang, Y.; Blom, P. W. M. Electron and Hole Transport in Poly(fluorene-benzothiadiazole). *Appl. Phys. Lett.* **2011**, *98*, 143504.
(66) Takada, M.; Nagase, T.; Kobayashi, T.; Naito, H. 19−5: Late-News Paper: Characterization of Carrier Transport Properties in Working Polymer Light-Emitting Diodes. *Dig. Technol. Pap.-Soc. Inf. Dispersion Symp.* **2019**, *50*, 263−266.
(67) Bird, M. J.; Bakalis, J.; Asaoka, S.; Sirringhaus, H.; Miller, J. R. Fast Holes, Slow Electrons, and Medium Control of Polaron Size and Mobility in the DA Polymer F8BT. *J. Phys. Chem. C* **2017**, *121*, 15597−15609.
(68) Bulkin, B. J. The Infrared Spectra of Complex Molecules. *J. Polym. Sci., Polym. Lett.* **1981**, *19*, 520−521.
(69) Fraenkel, G.; Belford, R. L.; Yankwich, P. E. Decarboxylation of Malonic Acid in Quinoline and Related Media. *J. Am. Chem. Soc.* **1954**, *76*, 15−18.
(70) Liptay, W. Introduction to Infrared and Raman Spectroscopy. *Angew. Chem.* **1965**, *77*, 744−745.

https://doi.org/10.1021/acsami.2c07610
ACS Appl. Mater. Interfaces 2022, 14, 38270−38280